Estuarine, Coastal and Shelf Science 223 (2019) 115–128

Contents lists available at ScienceDirect

Estuarine, Coastal and Shelf Science

journal homepage: www.elsevier.com/locate/ecss

Between the tides: Modelling the elevation of Australia's exposed intertidal zone at continental scale

Robbi Bishop-Taylor[a,*], Stephen Sagar[a], Leo Lymburner[a], Robin J. Beaman[b]

[a] Geoscience Australia, Cnr Jerrabomberra Ave and Hindmarsh Drive, Symonston, ACT, 2609, Australia
[b] College of Science and Engineering, James Cook University, Cairns, QLD, 4870, Australia

ARTICLE INFO

Keywords:
Digital elevation model
Intertidal zone
Remote sensing
Continental-scale
Tidal modelling
Australia
Landsat

ABSTRACT

The intertidal zone represents a critical transition between marine and terrestrial ecosystems, supporting a complex mosaic of highly productive and biologically diverse habitats. However, our understanding of these important coastal environments is limited by a lack of spatially consistent topographic data, which can be extremely challenging and costly to obtain at continental-scale. Satellite remote sensing represents an important resource for monitoring extensive coastal zones. Previous approaches to modelling the elevation of the intertidal zone using earth observation (EO) data have been restricted to small study regions or have relied on manual image interpretation, thus limiting their ability to be applied consistently over large geographic extents. In this study, we present an automated open-source approach to generate satellite-derived elevation data for over 15,387 km^2 of intertidal terrain across the entire Australian coastline. Our approach combines global tidal modelling with a 30-year time series archive of spatially and spectrally calibrated Landsat satellite data managed within the Digital Earth Australia (DEA) platform. The resulting National Intertidal Digital Elevation Model (NIDEM) dataset provides an unprecedented three-dimensional representation of Australia's vast exposed intertidal zone at 25 m spatial resolution. We validate our model against LiDAR, RTK GPS and multibeam bathymetry datasets, finding that modelled elevations are highly accurate across sandy beach (± 0.41 m RMSE) and tidal flat environments (± 0.39 m RMSE). Model performance was least accurate (± 2.98 m RMSE) within rocky shores and reefs and other complex coastal environments with extreme and variable tidal regimes. We discuss key challenges associated with modelling intertidal elevation including tidal model performance and biased observations from sun-synchronous satellites, and suggest future directions to improve the accuracy and utility of continental-scale intertidal elevation modelling. Our model can be applied to tidally-influenced coastal environments globally, addressing a key gap between the availability of sub-tidal bathymetry and terrestrial elevation data.

1. Introduction

The intertidal zone - the area of coastline periodically exposed and inundated by tides - represents a critical transition between marine and terrestrial ecosystems. Intertidal environments support a complex mosaic of extremely productive and biodiverse habitats ranging from extensive tidal mudflats, sandy beaches, fringing coral reefs and steep rocky cliffs (Banks et al., 2005; Luijendijk et al., 2018). Due to the influence of tidal processes, organisms inhabiting the intertidal zone are typically adapted to extremely dynamic conditions and display strong zonation by elevation along the environmental gradient from permanently to occasionally inundated terrain (Bearup and Blasius, 2017). Because of their high ecological diversity and productivity, intertidal zones serve as key feeding grounds for many endangered shorebird species that use them as critical 'stop-over' points while undertaking cross-continental migrations (Murray et al., 2015; Xia et al., 2017). In addition to their ecological value, intertidal zones also provide many economically significant ecosystem services, including nutrient cycling and carbon storage (Chmura et al., 2003; Billerbeck et al., 2006), storm surge protection (Temmerman et al., 2013), and natural resources for recreational and commercial use (Barbier et al., 1997; Chen et al., 2016). Intertidal zones, however, are also among the world's most vulnerable and threatened ecosystems, with land reclamation, changes in river sediment balances and coastal erosion representing key threatening processes responsible for a global reduction in intertidal extent of up to 16% between 1984 and 2016 (Murray et al., 2018). Given their

* Corresponding author.
E-mail addresses: Robbi.BishopTaylor@ga.gov.au (R. Bishop-Taylor), Stephen.Sagar@ga.gov.au (S. Sagar), Leo.Lymburner@ga.gov.au (L. Lymburner), robin.beaman@jcu.edu.au (R.J. Beaman).

https://doi.org/10.1016/j.ecss.2019.03.006
Received 18 October 2018; Received in revised form 12 March 2019; Accepted 12 March 2019
Available online 20 March 2019

low relief, intertidal zones are also likely to be disproportionately affected by global sea-level rise, which is expected to accelerate throughout the 21st century (Galbraith et al., 2002; Kirwan and Megonigal, 2013; Li and Gong, 2016).

Understanding, predicting and managing the impacts of these processes on intertidal ecosystems requires detailed data on the distribution and structure of these habitats across ecologically relevant spatial extents. However, the three-dimensional topography of the intertidal zone remains poorly mapped globally (Eakins and Grothe, 2014; Tseng et al., 2017). Due to the impermeability of water to radar transmission and a lack of repeated observations over tidally-influenced terrain, global digital elevation models (DEMs) produced using Synthetic Aperture Radar (e.g. TerraSAR-X/TanDEM-X WorldDEM and Shuttle Radar Topography Mission DEM or SRTM) or stereo-pair optical imagery (e.g. Aster GDEM) are typically restricted to the terrestrial domain (Eakins and Grothe, 2014; Tseng et al., 2017). Similarly, intertidal zones are regularly omitted from bathymetric models produced using acoustic techniques due to the difficulty of surveying safely from vessels in shallow coastal waters (Hogrefe et al., 2008; Eakins and Grothe, 2014; Weatherall et al., 2015). When combined with hazardous ground survey conditions caused by dynamic tidal processes, this has resulted in a significant gap in the elevation data available across the land-sea interface (Hogrefe et al., 2008; Eakins and Grothe, 2014). Airborne Light Detection and Ranging (LiDAR) bathymetry surveys have shown promise as an approach to address this gap, being capable of rapidly generating accurate, high-resolution bathymetry data at depths of up to 70 m in clear water (Su et al., 2008). However, the reliability of these systems can be strongly influenced by turbidity and breaking white water that frequently affect shallow coastal zone waters, and their high acquisition cost usually limits applications to local- or regional-scales (Su et al., 2008; Gao, 2009; Klemas, 2011).

Temporal 'waterline' methods based on satellite remote sensing represent an alternative approach to modelling the elevation of the intertidal zone (Mason et al., 1997; Chen and Rau, 1998). The rise and fall of the ocean can be used to describe the three-dimensional topography of the coastline by mapping the location of the waterline as a series of topographic contours that cover a range of tidal stages (Zhao et al., 2008; Tseng et al., 2017). Assuming that each waterline represents a constant elevation relative to mean sea level (MSL), these contours can be tagged with tide heights and then interpolated to produce a DEM covering the elevation range between the highest and lowest observed tide (Ryu et al., 2008). Satellites such as the United States Geological Survey (USGS) Landsat mission have continuously monitored coastal zones globally since 1972, providing the temporal depth and resolution required to obtain dense observations across the full tidal range (Boak and Turner, 2005; Gens, 2010). Accordingly, temporal stacks of satellite imagery have been combined with tidal modelling to produce tidally-tagged time series of the coastline for DEM generation (e.g. Mason et al., 1997; Chen and Rau, 1998; Ryu et al., 2008; Zhao et al., 2008; Chen and Chang, 2009; Liu et al., 2013a, 2013b; Xu et al., 2016; Tseng et al., 2017). However, due to challenge of extracting waterline contours from large numbers of remotely-sensed images, previous approaches have extracted waterlines from a limited selection of images using manual digitisation and visual interpretation (e.g. Chen and Rau, 1998; Zhao et al., 2008; Liu et al., 2013b; Chen et al., 2016). Although these manually digitised contours can produce highly accurate DEMs (e.g. less than 0.4 m RMSE compared to LiDAR; Liu et al., 2013b), this manual process introduces subjectivity, is impractical to apply at a continental-scale, and is restricted by availability of high quality observations covering the entire tidal range.

There is a recognised need for more objective and robust approaches to waterline extraction and intertidal DEM generation that can be applied consistently across space and time (Boak and Turner, 2005). Such approaches are likely to require leveraging the full temporal record of available global-extent earth observation (EO) data. While satellite data with long temporal records such as the Landsat archive were formerly prohibitively expensive to apply at continental-scale, the USGS free-data policy in 2008 has significantly lowered barriers to obtaining EO data (Woodcock et al., 2008; Wulder et al., 2012). More recently, the creation of archives of analysis-ready data or ARD (Dwyer et al., 2018) combined with high-performance computing platforms have provided unprecedented access to petabytes of geometrically and spectrally calibrated satellite imagery (Lewis et al., 2016). ARD archives and analysis platforms such as Digital Earth Australia (Dhu et al., 2017), Google Earth Engine (Gorelick et al., 2017) and the upcoming Copernicus Data and Information Access Services provide satellite observations that can be analysed and compared consistently across space and time. This has driven a new wave of scientific applications that leverage multiple decades of data to analyse extremely large areas of the Earth's surface (e.g. Mueller et al., 2016; Hermosilla et al., 2017; Bugnot et al., 2018; Egorov et al., 2018; Luijendijk et al., 2018). These developments make it practical for the first time to implement automated waterline extraction and intertidal elevation modelling at the continental-scale.

In this study, we present an open-source workflow for deriving elevation data for the intertidal zone of Australia. We leverage the full 30-year archive of analysis-ready Landsat data managed within the Digital Earth Australia (DEA) platform that provides spatially and spectrally calibrated EO data, enabling time-series analysis on a per-pixel basis across the entire Australian continent. We combine this archive with a newly developed multi-resolution tidal modelling framework that accurately associates each satellite observation with modelled tide heights. The resulting National Intertidal Digital Elevation Model (NIDEM; Bishop-Taylor et al., 2018) is a continental-scale dataset providing the first 25 m resolution, three-dimensional representation of Australia's exposed intertidal environments including tidal flats, sandy beaches and shores, and rocky shores and reefs. We anticipate that NIDEM will complement existing intertidal extent products and support a new suite of use cases that require a more detailed understanding of the three-dimensional topography of the intertidal zone, such as hydrodynamic modelling, coastal risk management and ecological habitat mapping projects.

2. Methods

2.1. Relative intertidal extents

The foundation of NIDEM is the continental-scale Intertidal Extents Model (ITEM v1.0) developed by Sagar et al. (2017), derived from a 30-year time series archive of Landsat observations. The Landsat archive is managed within the Digital Earth Australia (DEA) platform, combining high performance computing with the concept of spatiotemporally consistent ARD (Dhu et al., 2017). These data are processed to surface reflectance utilising a standardised atmospheric and geometric correction workflow to enable operational analysis (Lewis et al., 2016). The ITEM process is based on sorting all observations in the Landsat archive by tide height, binning observations into ten percent intervals of the observed tidal range, then mapping the typical location of the waterline across a range of tidal stages using Normalised Difference Water Index composite images (NDWI; McFeeters, 1996). NDWI is a remote sensing index designed to detect open water by taking advantage of the high reflectance of visible green light and low reflectance of near-infrared radiation (NIR) by water, and the high reflectance of NIR by dry soil and terrestrial vegetation:

$$NDWI = \frac{(Green - NIR)}{(Green + NIR)}$$

Although NDWI has been used extensively to monitor the intertidal zone (e.g. Murray et al., 2012; Dhanjal-Adams et al., 2016; Fan et al., 2018; Luijendijk et al., 2018), NIR bands can be affected by white water near the land-water boundary (Kelly and Gontz, 2018; Pardo-Pascual et al., 2018). Other indices such as the Modified Normalised Difference Water Index (MNDWI; Xu, 2006) have shown promise for monitoring

the intertidal zone by utilising short-wave infrared (SWIR) in place of NIR (e.g. Wang et al., 2018; Xu, 2018). However, SWIR-based indices have been found to significantly misrepresent the location of the waterline across exposed tidal flats where water remains during ebb tides (Ryu et al., 2002, 2008). To ensure waterlines could be consistently extracted from imagery across tidal stages and intertidal environments that included extensive tidal flats, NDWI was selected and applied to all Landsat observations within each ten percent tidal interval. These individual NDWI layers were then combined into composites for each tidal interval by taking the median NDWI value per pixel, and classified to produce water vs. non-water layers that represented typical waterlines locations from the lowest to the highest observed tides (Fig. 2a).

In this study, we further develop the initial model (ITEM v1.0) described in Sagar et al. (2017) by leveraging improvements in the tidal modelling framework that underpins the ITEM modelling process. The tidal modelling used in ITEM v1.0 was constrained spatially into 1° × 1° resolution image cells (approximately 110 × 110 km at the equator), with a single tidal height assigned to the centre of each Landsat image based on its time of acquisition. This spatially consistent image cell grid implicitly assumed that tidal heights did not vary across the 1° × 1° cell extent, and that a single modelled tide height per cell could adequately reflect complex tidal dynamics operating at a range of spatial scales. This assumption resulted in sometimes severe model discontinuities at some cell boundaries and poor modelling performance in complex estuaries and other coastal areas characterised by high tidal flux (Sagar et al., 2018, 2017). ITEM v2.0 was developed by replacing the spatially consistent image cell grid with a multi-resolution tidal framework developed by Sagar et al. (2018). The framework uses partitioning methods to allow spatial variability in the tidal model to drive the size and locations of a Voronoi polygon mesh. The 306 resulting tidal modelling polygons (Fig. 1) are then used as analysis units for the ITEM modelling process, with tide height predictions defined at the nodes of each Voronoi cell. We used the Oregon State University Tidal Prediction Software (OTPS) TPX08 model (Egbert and Erofeeva, 2010, 2002) to predict tide heights. OTPS tidal modelling has been used successfully for continental-scale intertidal modelling applications in both Asia and Australia (Murray et al., 2012; Dhanjal-Adams et al., 2016). The model consists of a multi-resolution bathymetric grid with a 1/6° resolution (~18 × 18 km at the equator) solution in the global open ocean and a 1/30° local resolution (~4 × 4 km) solution to improve modelling in complex shallow-water environments, and has been validated to ~12 cm root mean square error (RMSE) misfit against the Australian Hydrographic Office AusTides tide gauge records (Rogers et al., 2017). The study area for ITEM v2.0 and NIDEM has been extended to cover the Great Barrier Reef and the entire Australian coastline, including Tasmania. The use of the multi-resolution tidal model has produced significant improvements in the coverage and resolution of the relative intertidal extents model, most notably in the offshore regions of northern Australia and the Kimberley coast in north-western Australia.

2.2. Unfiltered absolute elevation

ITEM v2.0 details the relative extent of the intertidal zone at intervals of the observed tidal range. As such, it provides topography of the exposed intertidal surface but not an absolute elevation measure. To derive absolute elevations, we used the *find_contours* function from *scikit.measure* (Van der Walt et al., 2014) to extract waterline contours (Fig. 2b) along the boundary of each of the ten percent tidal interval boundaries in ITEM v2.0 (Fig. 2b). This contour extraction method uses the 'marching squares' algorithm (Lorensen and Cline, 1987) to identify precise contour boundaries in a two-dimensional array by linearly interpolating between adjacent pixel values. For each interval boundary,

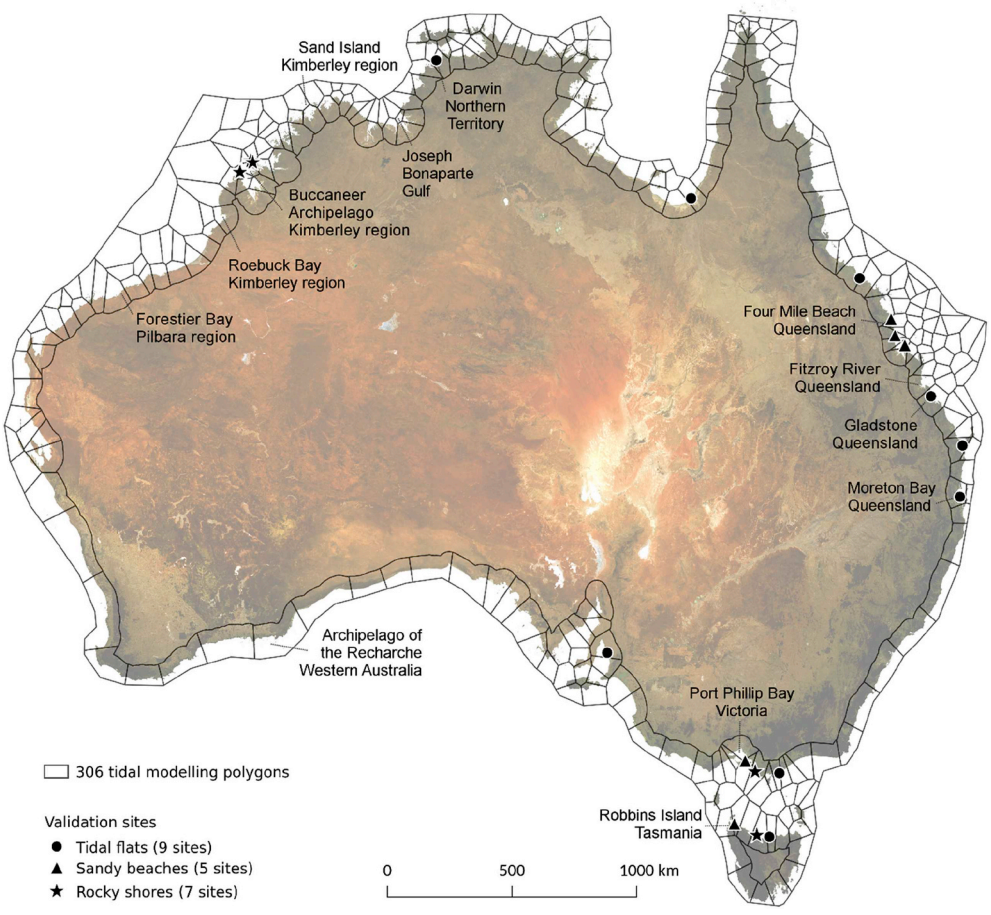

Fig. 1. Map of the continental-scale Australian study area, showing the location of the 306 tidal modelling polygons and validation sites for tidal flats (9 sites; circles), sandy beaches and shores (5 sites; triangles), and rocky shores and reefs (7 sites; stars). Labels highlight locations referred to in this work. Image underlay is a composite of all Landsat 8 satellite observations across Australia (Roberts et al., 2017).

we computed the median tidal height of the ensemble of all Landsat observations originally used to derive the corresponding median composite NDWI layer, and assigned this height as the contour's z-value. To convert contours to continuous elevation data rasters, we first extracted x, y and z point data for each contour vertex, and used these points as inputs for interpolation. We used the *griddata* interpolation function from *scipy.interpolate* (Jones et al., 2014), and selected the 'linear' interpolation method to ensure that interpolated elevation values preserved the tidal interval boundaries of ITEM v2.0. This interpolation method computes a Triangulated Irregular Network or Delaunay triangulation of the input data using the Quickhull algorithm (Barber et al., 1996), before performing linear barycentric interpolation on each triangle to estimate new values for each pixel (Fig. 2c). We set the output resolution of the interpolation to 25 × 25 m, producing two-dimensional elevation arrays that matched the cell size and extent of the original ITEM v2.0 layers and input Landsat observations. As elevations for the lowest and highest ITEM v2.0 intervals could not be correctly interpolated because they had no lower or upper bounds, we constrained the interpolated elevation arrays to the observed intertidal zone by masking out pixels located within consistently inundated (ITEM v2.0 interval 0) and consistently non-inundated terrain (interval 9). This resulted in a set of 306 'unfiltered' intertidal elevation datasets with elevations in metre units relative to modelled MSL (approximately equivalent to the Australian Height Datum or AHD). To facilitate future re-analysis such as the application of alternative interpolation methods, waterline contours were exported as shapefiles.

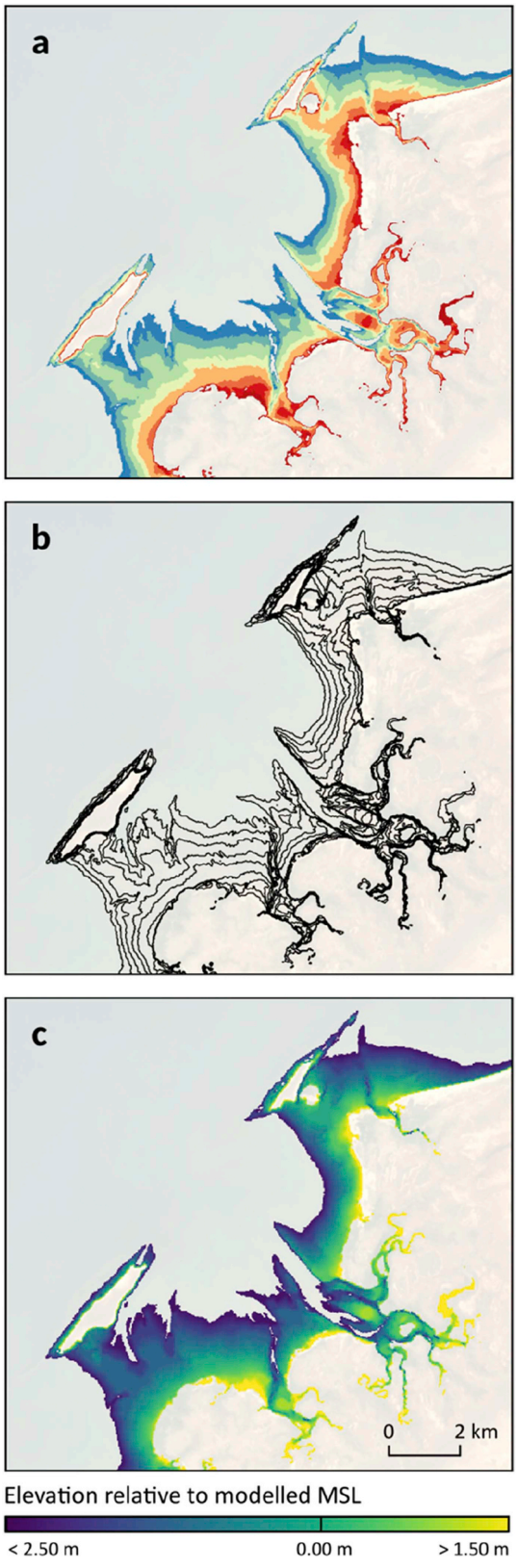

Fig. 2. The process followed to extract and interpolate waterline contours for NIDEM for an example area (Forestier Bay in the Pilbara region of Western Australia). Boundaries of each (a) ten percent interval of the observed tidal range from ITEM v2.0 (colours from blue to red indicate pixels inundated at increasingly high tide) were used to (b) extract contours depicting the typical location of the land-water boundary across the 30-year Landsat time series. These contours were assigned the median of all modelled tide heights attributed to the ensemble of Landsat images used to generate each tidal interval. The resulting tidally-tagged contours were used to generate (c) continuous elevation surfaces using triangulated irregular network (TIN) interpolation. (For interpretation of the references to colour in this figure legend, the reader is referred to the Web version of this article.)

2.3. Filtered absolute elevation

The accuracy of intertidal elevation modelling approaches based on waterline extraction and tidal modelling is dependent on the ability of a tidal model to correctly assign and sort satellite observations by tidal height (Liu et al., 2013b; Sagar et al., 2017). This assumption may not hold in areas that have undergone significant geomorphological change across the 30-year time series, or where modelled tidal heights differ from actual tidal heights due to inherent model error (Ryu et al., 2008; Sagar et al., 2017). To identify potentially invalid elevation values, we used a 'confidence' layer developed as part of ITEM v2.0. The ITEM confidence layer is based on the per-pixel variance in NDWI values for the ensemble of images used to produce each ten percent tidal interval composite. We used a conservative maximum threshold of 0.25 NDWI standard deviation to mask out over 1980 km^2 of intertidal pixels (5.5% of the total 'unfiltered' dataset) where tidal processes poorly explained inundation patterns across the 30-year time series.

The robust median compositing method used to combine NDWI images in ITEM 2.0 ensured that the input relative intertidal extent layers were relatively free of artefacts including outliers, poorly removed cloud edges and sunglint that commonly affect coastal remote sensing imagery (Sagar et al., 2017; White et al., 2014). However, composite layers produced from multiple satellite observations can still be susceptible to artefacts in regions with high cloud cover or fewer observations in the Landsat archive (Flood, 2013; White et al., 2014; Roberts et al., 2017). For NIDEM, this typically manifested as pixels located either inland of the coastal zone or in areas of deeper water incorrectly mapped as intertidal terrain in data poor areas of the Australian coastline. To remove these artefacts, we restricted NIDEM layers to a 50 m elevation range centred on MSL. This large range relative to the maximum Australian tidal range of over 11 m (Solihuddin et al.,

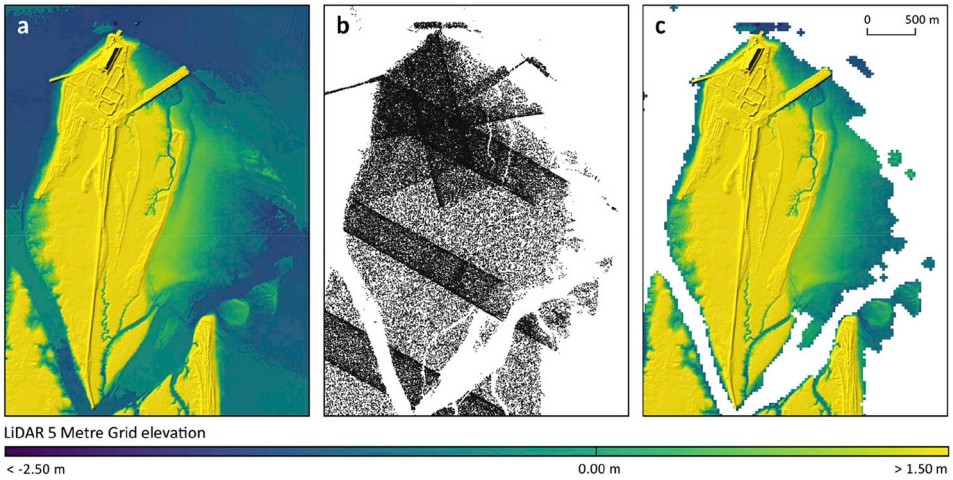

Fig. 3. The process followed to extract usable validation data for the intertidal zone from the (a) bare-earth LiDAR 5 Metre Grid dataset (Geoscience Australia, 2015) for an example area affected by tidal-stage artefacts (Gladstone in central Queensland; dark colours indicate greater depth). For each validation site, (b) xyz LiDAR point clouds were extracted and tagged with tidal heights using the OTPS tidal model for the exact moment each point was acquired. Tidally tagged points located above the water level at the time of LiDAR acquisition were rasterised and used to produce a mask indicating the location of (c) non-inundated intertidal terrain in the LiDAR DEM.

2016) was selected to remove obvious false positives without eliminating true intertidal terrain. We used elevation data from Australia's SRTM-derived 1 Second Digital Elevation Model (Gallant et al., 2010) to mask out approximately 402 km^2 of terrain with elevations greater than 25 m above MSL (1.1% of the total 'unfiltered' dataset). Bathymetry data from the national 250 m Australian Bathymetry and Topography Grid (Whiteway, 2009) and the 30 m gbr30 and nthaus30 high-resolution depth models for the Great Barrier Reef and Northern Australia (Beaman, 2018a, 2018b) were used to mask out pixels located at depths of greater than −25 m in all three datasets. This removed over 18,325 km^2 of misidentified intertidal terrain (50.7% of the total 'unfiltered' dataset) which was largely concentrated (i.e. 9571 and 4574 km^2, or 26.5 and 12.7%) in two data-poor tidal modelling polygons located off the Archipelago of the Recherche in southern Western Australia. All layers were reprojected to the resolution (25 × 25 m) and projection system (GDA94 Australian Albers, EPSG:3577) of the NIDEM layers using bilinear resampling prior to masking. The resulting masked layers were exported as "filtered" elevation datasets, while the combined mask (i.e. ITEM confidence, bathymetry and elevation limits) was exported as "mask" layers to facilitate re-analysis through the application of customised masking criteria.

2.4. Tidal range coverage

To evaluate the representativeness of NIDEM data compared to the full tidal range, we compared the spread of tidal heights coincident with the input Landsat imagery against the full range of modelled tide heights present within each tidal modelling polygon. We calculated three indices: spread (the proportion of the full modelled tidal range observed by Landsat), low tide offset (the proportion of the lowest tidal heights not observed by Landsat) and high tide offset (the proportion of the highest tidal heights not observed by Landsat). The variations in these indices in different regions relate to the sun-synchronous nature of observations from satellites such as the Landsat series, and are discussed in the following section.

2.5. Validation

To assess the accuracy of NIDEM, we validated 'filtered' elevations at multiple sites and intertidal environments along the Australian coastline. We used the nationally-consistent coastal 'Smartline' geomorphic and stability map (Sharples et al., 2009) to identify the dominant intertidal landform type for each validation site. These landforms were summarised into three distinct intertidal categories: sandy beaches (including sandy and mixed sand beach and shores), tidal flats (including sand, mud and undifferentiated tidal flats) and rocky reefs and shores (including hard bedrock shores). We obtained validation data from three different elevation and bathymetry data sources: the DEM of Australia derived from LiDAR 5 Metre Grid (Geoscience Australia, 2015), point elevation data collected from Real Time Kinematic (RTK) GPS surveys (Danaher and Collett, 2006; HydroSurvey Australia, 2009), and 1.0 m resolution multibeam bathymetry surveys (Solihuddin et al., 2016). Validation datasets were processed as described below and pooled across sample sites for each intertidal environment type. We compared modelled (i.e. NIDEM) and observed (i.e. validation) data using the *pandas* Python package (McKinney, 2011) by calculating RMSE accuracy and two correlation coefficients (Pearson's and Spearman's). Pearson's correlation was used to assess whether NIDEM accurately modelled absolute elevation by evaluating the linear relationship between modelled and observed values. Spearman's correlation assessed whether modelled elevations were monotonically related to validation elevations, allowing us to evaluate if at a minimum the relative – not absolute – topography of the intertidal zone was captured by NIDEM. For example, this could assess to what extent actual low tide terrain was correctly identified as low tide terrain in NIDEM even if absolute elevations from the tidal model were incorrect.

2.5.1. LiDAR validation data

The bare-earth LiDAR 5 Metre Grid covers over 245,000 km^2 of predominantly coastal terrain across eastern and northern Australia with accuracy of better than 0.30 m (95% confidence, AHD vertical datum; Geoscience Australia, 2015). However, the dataset has sporadic coverage of the intertidal zone, with some coastal regions affected by elevation discontinuities caused by aerial surveys flown at different tidal stages (e.g. Fig. 3a). To extract usable validation data for the intertidal zone in areas affected by these artefacts, we developed a novel LiDAR point-cloud tidal tagging approach to identify non-inundated intertidal terrain in the DEM. Fourteen validation sites (Fig. 1) were identified within randomly selected tidal modelling polygons based on the availability of extensive intertidal terrain in both NIDEM and LiDAR datasets. LiDAR 5 Metre Grid data was extracted for each of these sites and reprojected using average resampling to match the NIDEM resolution and projection system with the *gdalwarp* image reprojection and warping utility (GDAL/OGR contributors, 2018). For eight of the fourteen validation sites affected by tidal artefacts, we used the *las2txt* tool from *LAStools* software (Isenburg, 2018) to extract a 1% sample of xyz points and associated metadata from the . las format LiDAR point-cloud datasets used to generate the LiDAR 5 Metre Grid (Fig. 3b). For each extracted LiDAR point, we used the OTPS tidal model (Egbert and Erofeeva, 2002, 2010) to compute a tidal height relative to MSL based on the point's time of acquisition timestamp. By rasterising all points with z-values (elevations) greater than the instantaneous tidal height at the time of LiDAR acquisition (plus a 0.15 m buffer to account for point

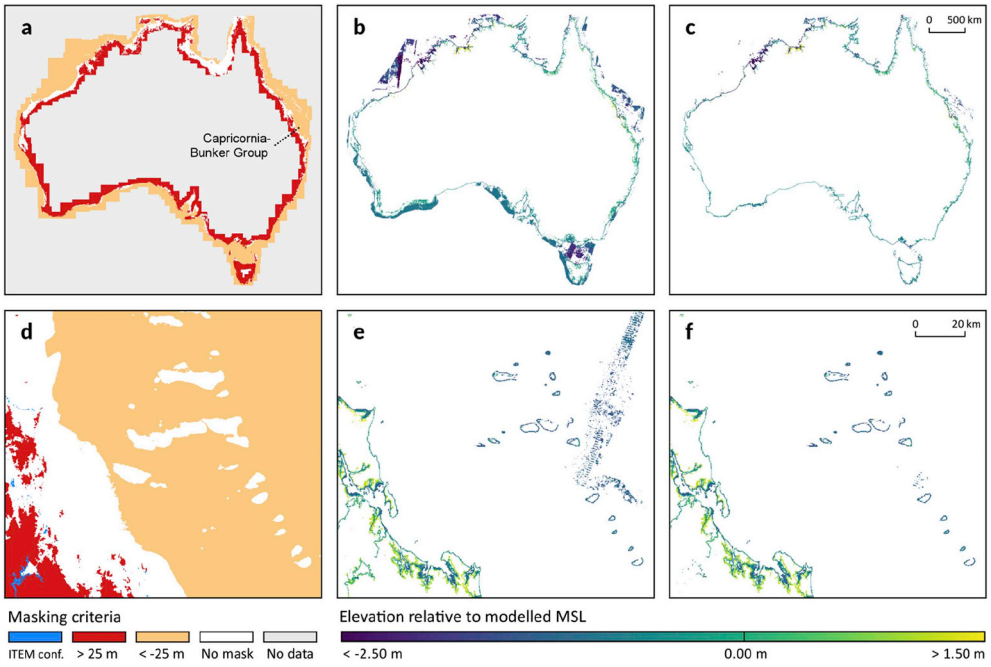

Fig. 4. The output NIDEM layers at continental-scale (top row; aggregated to 2500 m pixel size for visualisation) and local-scale (bottom row; focused on the Capricornia-Bunker Group of reefs in central Queensland). The NIDEM 'mask' layer (a, d) highlights pixels flagged as exhibiting poor tidal model performance or significant geomorphic change across the 30-year time series based on the ITEM confidence layer (blue), pixels located above 25 m elevation (red) or pixels located below −25 m depth (orange). The effect of applying this mask can be seen by comparing the NIDEM 'unfiltered' layer (b, e) against the NIDEM 'filtered' layer (c, f) which was cleaned by masking by NIDEM 'mask'. (For interpretation of the references to colour in this figure legend, the reader is referred to the Web version of this article.)

cloud noise), we produced a binary mask representing non-inundated terrain in the LiDAR DEM. This mask was cleaned to remove remaining noise by using the *scipy.ndimage* mathematical morphology *binary_opening* and *binary_closing* tools (Jones et al., 2014). Binary opening removed isolated pixels by 'eroding' (shrinking the data area by one pixel) and subsequently 'dilating' (expanding the remaining data area by one pixel) the mask layer, while binary closing filled gaps by first dilating then eroding the array (Serra, 1983). The resulting cleaned mask was then used to extract intertidal validation data from the original LiDAR 5 Metre Grid (Fig. 3c).

2.5.2. RTK GPS validation data

RTK GPS transect elevation survey data covering tidal flats at East Point in Mindal Bay, Darwin and Moreton Bay, Queensland (Fig. 1) were collected by HydroSurvey Australia (2009) and Danaher and Collett (2006). Point data with elevations in AHD (stated vertical accuracy of ± 0.02 m) from both surveys were rasterised to match the NIDEM resolution and projection system by taking the average elevation value when multiple GPS points fell within a single Landsat pixel.

2.5.3. Multibeam bathymetry validation data

Multibeam bathymetry validation data were obtained for five sites in the Buccaneer Archipelago in the southern Kimberley region (Cockatoo Island, east Tallon Island, west Tallon Island, Waterflow and Irvine/Bathurst Islands; Fig. 1). The data consisted of 1 m resolution gridded AHD reef elevations measured using an Odom ES3 multibeam echo sounder with a Trimble RTX satellite subscription (± 0.02 m positioning accuracy; Solihuddin et al., 2016). All multibeam data were resampled to the NIDEM resolution and projection system using average resampling.

3. Results and discussion

In this study, we present an automated approach to generating satellite-derived elevation data for over 15,387 km^2 of exposed intertidal

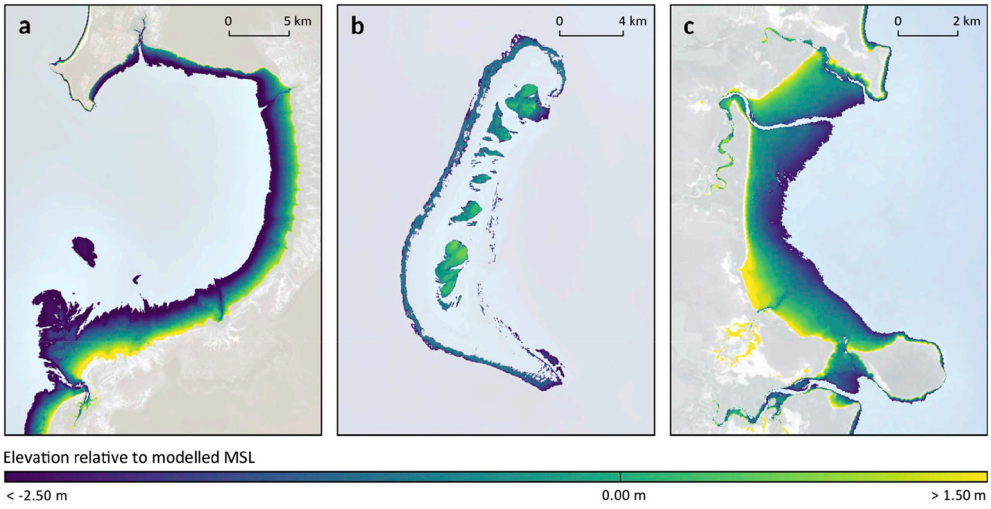

Fig. 5. Examples of the 'filtered' NIDEM intertidal elevation data, including (a) Roebuck Bay and (b) Sand Island in the Kimberley region of north-western Western Australia, and (c) Four Mile Beach in the Isaac region of central Queensland.

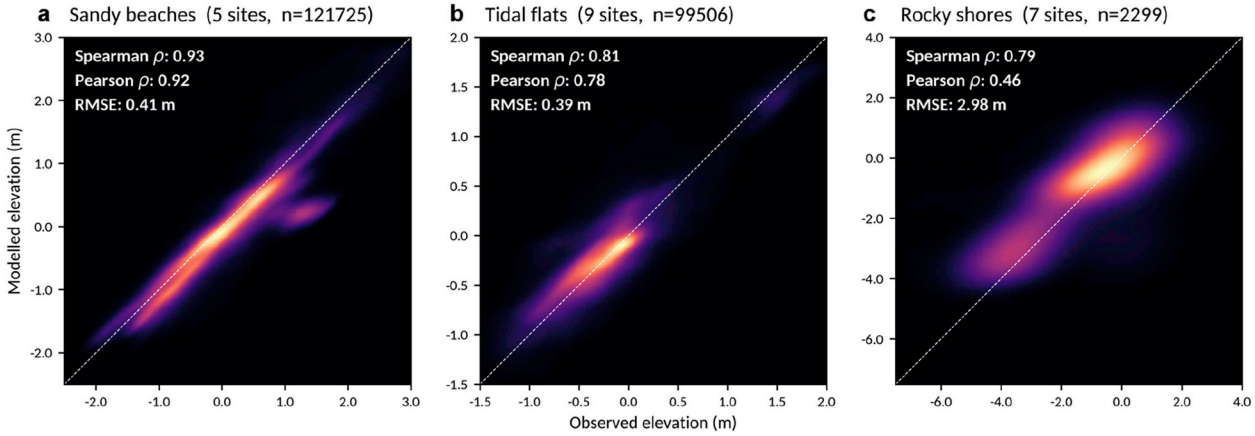

Fig. 6. Validation results for NIDEM intertidal elevation compared across (a) five sandy beach and shore sites, (b) nine tidal flat sites, and (c) seven rocky shore and reef sites. Modelled (NIDEM 'filtered' elevations) and observed (validation) datasets are compared as density heatmaps with associated correlation coefficients (Spearman and Pearson correlation) and root mean square error (RMSE). Validation data was sourced from the LiDAR 5 Metre Grid (Geoscience Australia, 2015), Real Time Kinematic (RTK) GPS surveys from Darwin, Northern Territory (HydroSurvey Australia, 2009) and Moreton Bay, Queensland (Danaher and Collett, 2006), and 1.0 m resolution multibeam bathymetry surveys across the southern Kimberley region, Western Australia (Solihuddin et al., 2016).

sandy beaches and shores, tidal flats and rocky shores and reefs across the entire Australian coastline (Bishop-Taylor et al., 2018, Figs. 4 and 5). Intertidal elevations in metre units relative to modelled MSL ranged between −5.57 m and +3.41 m, with the largest spread of elevations located in the macrotidal Kimberley region in north-western Australia (7.69 m) and the central Queensland coast of eastern Australia (4.58 m). Although previous studies have mapped the extent of the intertidal zone both globally (Murray et al., 2018) and at continental-scale across Southeast Asia (Murray et al., 2012) and Australia (Dhanjal-Adams et al., 2016; Sagar et al., 2017), to our knowledge NIDEM represents the first continental-scale DEM of the intertidal zone.

3.1. Model performance across sandy beaches and shores

Elevation values from NIDEM agreed well with LiDAR 5 Metre Grid validation datasets across sandy beach and shore intertidal environments. Validation elevations for 121,725 paired pixels pooled across five sites along the Australian coastline were strongly correlated with NIDEM (Pearson's ρ = 0.92, Spearman's ρ = 0.93), resulting in a low RMSE of ± 0.41 m which approached the vertical accuracy of the contributing LiDAR surveys (i.e. < 0.30 m; Fig. 6a, Table 1). Our results compare favourably to more manual, non-automated approaches to waterline delineation, including the construction of intertidal DEMs for a 1,267 km^2 portion of the Dongsha sandbank in China's Jiangsu Province using on-screen digitisation of MODIS and Landsat imagery (Liu et al., 2013a, 2013b). The Dongsha sandbank DEMs exhibited similarly strong correlations with LiDAR validation data (R^2 = 0.92), with vertical accuracies of between ± 0.45–0.62 m RMSE depending on the number of input satellite images used to generate the DEMs. Tseng et al. (2017) achieved similar correlations (Pearson's ρ = 0.93) and vertical accuracies (RMSE of ± 0.48 m) for tidal gauge-based validation of an intertidal DEM produced for the Hsiang-Shan Wetland in Taiwan using

Table 1
Sites used for validating NIDEM 'filtered' intertidal elevation data, including LiDAR data from the DEM of Australia derived from LiDAR 5 Metre Grid (Geoscience Australia, 2015) for 14 sites, elevation data collected from Real Time Kinematic (RTK) GPS surveys in Darwin, Northern Territory (HydroSurvey Australia, 2009) and Moreton Bay, Queensland (Danaher and Collett, 2006), and 1.0 m resolution multibeam bathymetry surveys for five sites in the southern Kimberley region, Western Australia (Solihuddin et al., 2016).

Validation site	Upper left extent	Lower right extent	Intertidal type	Validation type	N	Spearman's ρ	Pearson's ρ	RMSE
Robbins Island	144.77569 E 40.67712 S	145.05675 E 40.80737 S	Sandy beach	Lidar	39142	0.67	0.78	0.57
Isaac	149.41409 E 21.70398 S	149.49239 E 21.84647 S	Sandy beach	Lidar	33756	0.98	0.97	0.29
Mackay	149.18434 E 21.13746 S	149.24215 E 21.24583 S	Sandy beach	Lidar	31863	0.96	0.94	0.34
Western Port	145.26148 E 38.38818 S	145.35062 E 38.43080 S	Sandy beach	Lidar	8341	0.92	0.91	0.18
Rockhampton	149.88750 E 22.06129 S	149.93865 E 22.14870 S	Sandy beach	Lidar	8077	0.96	0.95	0.33
North Adelaide	138.33472 E 34.56679 S	138.44901 E 34.68063 S	Tidal flat	Lidar	31267	0.69	0.38	0.5
Fraser	152.87081 E 25.50751 S	152.93960 E 25.60194 S	Tidal flat	Lidar	20553	0.76	0.81	0.31
Kaurumba	140.74169 E 17.41546 S	140.91024 E 17.51980 S	Tidal flat	Lidar	15217	0.92	0.88	0.27
Whitsunday	147.68246 E 19.77447 S	147.79755 E 19.84846 S	Tidal flat	Lidar	13707	0.92	0.96	0.19
Launceston	146.73713 E 41.04967 S	146.83075 E 41.12098 S	Tidal flat	Lidar	8029	0.87	0.88	0.33
Shoal Inlet	146.73026 E 38.65132 S	146.80500 E 38.69423 S	Tidal flat	Lidar	5630	0.77	0.7	0.3
Gladstone	151.26893 E 23.84394 S	151.33706 E 23.89089 S	Tidal flat	Lidar	4699	0.88	0.78	0.66
Darwin	130.78231 E 12.43566 S	130.85607 E 12.37220 S	Tidal flat	RTK GPS	274	0.93	0.9	0.63
Moreton Bay	153.03747 E 27.51057 S	153.23696 E 27.27759 S	Tidal flat	RTK GPS	130	0.86	0.87	0.17
Ulverstone	146.08124 E 41.11277 S	146.11576 E 41.12340 S	Rocky shore	Lidar	575	0.89	0.91	0.46
Kilcunda	145.44656 E 38.54480 S	145.48469 E 38.55914 S	Rocky shore	Lidar	323	0.63	0.49	0.61
East Tallon	123.12726 E 16.40046 S	123.14075 E 16.41921 S	Rocky shore	Multibeam	557	0.54	0.6	1.22
Bathurst and Irvine	123.51438 E 16.02877 S	123.56828 E 16.05869 S	Rocky shore	Multibeam	443	0.58	0.22	6.53
Tallon west	123.11392 E 16.40050 S	123.12354 E 16.41947 S	Rocky shore	Multibeam	283	0.8	0.54	0.86
Waterflow	123.06432 E 16.42213 S	123.08308 E 16.43144 S	Rocky shore	Multibeam	85	0.86	0.59	1.85
Cockatoo Island	123.59018 E 16.08976 S	123.60608 E 16.10020 S	Rocky reef	Multibeam	33	−0.26	−0.19	0.46

22 years of Landsat imagery, although this DEM covered a relatively small extent of 16 km^2.

Poor modelling results occurred at a single site near Robbins Island in north-western Tasmania where accuracies were significantly lower (RMSE of ± 0.57 m) than the four other sites assessed (≤0.34 m; Table 1). This result was driven by a set of outlying values where NIDEM predicted low elevations between 0.0 and 0.5 m for an area of intertidal terrain with actual elevations ranging from 1.0 to 2.0 m (Fig. 6a). The Robbins Island site occurs on the boundary of two large shallow tidal basins (Boullanger Bay and Big Bay) and the intersection of three estuaries (the Duck, Montagu and Welcome Rivers), creating highly variable and unpredictable tidal conditions (Spruzen et al., 2008; Donaldson et al., 2012). This complex tidal regime challenges the application of any continental-scale tidal model, especially given that the individual instantaneous modelled tide heights used to assign elevations to waterlines are likely to rapidly decrease in accuracy with increasing distance from a given modelling point (Donaldson et al., 2012; Bell et al., 2016). In this study, we attempted to moderate the influence of spatially variable tidal conditions by adopting a multi-resolution tidal modelling framework that allowed local complexity in tides to drive the scale and boundaries of the model (Sagar et al., 2018). This minimised the distance between each satellite image and the locations used to calculate tides, resulting in a closer match between the tidal stage observed from space and the resulting attributed tide height. At the Robbins Island site, however, the resulting automatically derived tidal modelling polygons dissected Boullanger Bay in the west of the study site, causing an area of intertidal terrain within the bay to be assigned tidal heights that were more appropriate for the western Tasmanian open coast (see Appendix A1). Although this result highlights areas where the multi-resolution tidal modelling framework used in this study could be improved, results for other sites indicate that the approach provides a significant improvement over previous artefact-prone continental-scale modelling frameworks which used a regular 1 × 1° grid to assign tide heights to imagery (Sagar et al., 2018).

3.2. Model performance across tidal flats

We compared the performance of NIDEM across 99,506 pixels of tidal flat terrain at nine LiDAR 5 Metre Grid and RTK GPS survey sites across northern and southern Australia (Fig. 6b, Table 1). Although overall accuracies were high and consistent with sandy beach and shore sites (RMSE of ± 0.39 m), tidal flats exhibited slightly lower correlations overall (Pearson's ρ = 0.78, Spearman's ρ = 0.81). This result was expected given two interacting characteristics of tidal flat environments: their extensive, low-slope morphology and dynamism. Tidal flats are known to be highly variable, and can undergo significant geomorphic change in response to tidal processes and changes in sediment flux (Mason et al., 2010; Chen et al., 2016). Even small vertical changes in elevation in these gently sloping environments can produce large horizontal shifts in waterline locations (e.g. a 0.1 m change in elevation on a 1:500 slope tidal flat would result in a 50 m horizontal discrepancy in waterline position, equivalent to two Landsat pixels; Mason et al., 1995; Zhao et al., 2008). This presented a particular challenge to our composite-based approach, as coastal change at any point across our 30-year time-series would invalidate or reduce the accuracy of our waterline-derived modelled elevations. Previous studies have generated intertidal DEMs based on shorter temporal extents to reduce the influence of coastal change (e.g. Zhao et al., 2008; Liu et al., 2013b), however these approaches risk reducing the overall accuracy of modelled elevations by limiting available satellite observations and increasing the relative influence of natural variability and noise. To minimise the impact of geomorphic change while maximising our use of the Landsat archive, our approach used NDWI variance to mask individual pixels where tidal modelling poorly explained patterns of inundation (i.e. ITEM 2.0 confidence; Sagar et al., 2017). Although this approach effectively removed areas of significant coastal change, the choice of a single universal masking value (i.e. 0.25 NDWI standard deviation) unavoidably preserved areas of intertidal terrain subject to subtler, long-term geomorphic change. In these areas, NIDEM represents median or 'typical' elevation conditions across the 30-year time series.

Validation results for tidal flat environments revealed a distinct lack of modelled elevation data for the upper portion of the tidal range (e.g. between 0.5 and 1.3 m AHD; Fig. 6b). In tidal flats, the elevation zone above mean sea level is typically occupied by coastal wetlands including mangroves (Bunt et al., 1985; see Appendix A2). Although these vegetated intertidal communities are regularly inundated by tidal flows, patterns of inundation are difficult to observe from satellites due to the presence of dense canopy cover. This was particularly true for the NDWI index used to detect water in our model, which intentionally differentiates between open water and vegetated features based on their low and high reflectance of NIR radiation respectively (McFeeters, 1996). Although areas of exposed tidal flat terrain located behind mangroves were accurately modelled by NIDEM across our nine validation sites (i.e. areas above 1.3 m AHD in Fig. 6b), vegetative resistance to flowing water in mangrove, saltmarsh and other coastal wetland communities can cause significant hydrodynamic attenuation in tidal flow (Rodríguez et al., 2017; Montgomery et al., 2018). This would affect the spatial distribution of extracted waterlines by creating lags between tidal conditions and patterns of observed water. Due to these issues, caution should be applied when interpreting elevation values for intertidal regions on the landward side of coastal wetlands (e.g. Appendix A2), or other environments such as estuaries or areas influenced by artificial hydraulic structures where tidal flows may be similarly modified or restricted (Williams and Watford, 1997; Rodríguez et al., 2017).

3.3. Model performance across rocky shores and reefs

Although NIDEM produced accurate modelled elevations in sandy beaches and tidal flat environments, results were less accurate within rocky shore and reef environments. Modelled elevations (n = 2299) had a low Pearson's correlation of 0.46 and a high RMSE of ± 2.98 m vertical accuracy compared to LiDAR 5 Metre Grid and multibeam bathymetry data for seven validation sites (Fig. 6c, Table 1). Spearman's correlation was higher at 0.79, indicating that NIDEM largely captured the relative – but not absolute – topography of the surveyed sites. This poor result was driven by validations across five Buccaneer Archipelago reef sites within the southern Kimberley region, including one site (Cockatoo Island) where NIDEM elevations were negatively correlated with multibeam bathymetry (Pearson's and Spearman's ρ of −0.26 and −0.19; Table 1). The fringing reefs of the Buccaneer Archipelago are exposed to an extreme and dynamic tidal regime, including the largest tidal range of any coral reef system (approaching 11 m), with strong tidal currents that can exceed 18 km/h (Purcell, 2002; Solihuddin et al., 2016). Of particular relevance to the NIDEM approach, Lowe et al. (2015) observed significant asymmetry in tidal patterns on Tallon Island (one of the sites included in the NIDEM validation), with the shallow, elevated intertidal reef platform rapidly inundating over a short ~2 h period during flood tides, before draining slowly over ~10 h during ebb tides. The presence of 'trapped' water on the reef platform for extended periods caused areas of shallow exposed reef to

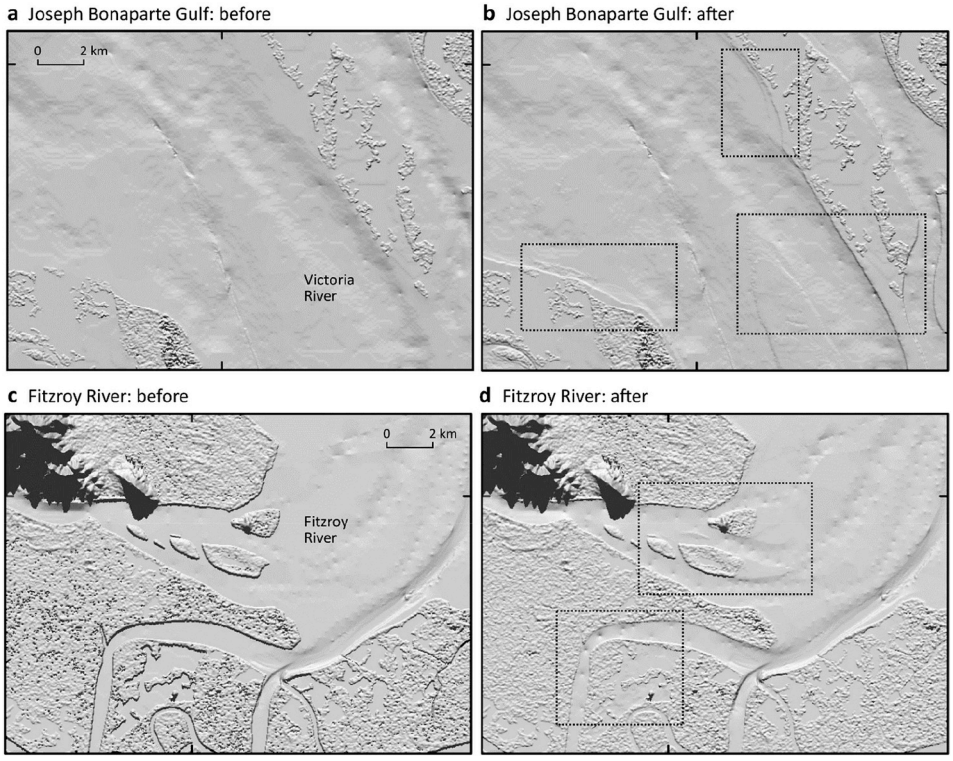

Fig. 7. Hillshaded nthaus30 depth model for Northern Australia (Beaman, 2018b) showing the Joseph Bonaparte Gulf and Victoria River area (a) before and (b) after the inclusion of NIDEM; hillshaded gbr30 depth model for the Great Barrier Reef (Beaman, 2018a) showing the Fitzroy River area of central Queensland (c) before and (d) after NIDEM. Note the NIDEM data subtly improves the stepping effect across the land/ocean interface and helps fill in the shallow reef flats around the islands and sand bars, resulting in better-defined river channels.

appear as permanently inundated terrain in the ensemble of input Landsat observations, and violated the assumptions of the input ITEM model by causing modelled tidal heights to become unsynchronised from actual water levels. Our results indicate that satellite-derived intertidal DEMs such as NIDEM are unlikely to produce accurate elevations in regions that exhibit significant unaccounted-for tidal asymmetry, or where the resolution or local accuracy of the tidal models used to assign tide heights is low. Increasing the accuracy of estimated tide heights in these locations will likely require accounting for finer-scale bathymetry and substrate conditions using locally specified hydraulic modelling (e.g. Lowe et al., 2015) that would be challenging to apply at the continental-scale. Future work should focus on developing additional methods for quantifying local tidal asymmetry and poor tidal modelling performance so that the accuracy and validity of satellite-derived intertidal DEMs can be quantitatively assessed for each pixel of intertidal terrain.

3.4. Potential of continental-scale intertidal elevation modelling

Our results demonstrate that satellite-derived elevation models based on waterline extraction can approach the accuracy of LiDAR for modelling the topography of tidal flats and sandy beach and shore environments. The NIDEM approach is particularly suitable for remote areas of inaccessible coastline (e.g. northern Australia) where higher-resolution approaches, such as shallow-water multibeam bathymetry or airborne bathymetric LiDAR, would be cost prohibitive or impractical. By providing an important 'missing link' between existing medium resolution terrestrial topographic and marine bathymetric datasets, we anticipate elevation data from NIDEM will contribute to unified coastal terrain models that combine best-available topography and bathymetry datasets into single continuous 'topobathy' datasets (Hogrefe et al., 2008). Examples are the nthaus30 depth model for Northern Australia (Beaman, 2018b) and the gbr30 depth model for the Great Barrier Reef (Beaman, 2018a) used to test the inclusion of NIDEM as source elevation data (Fig. 7). NIDEM data fills in the shallow reef flats around islands and sand bars within river channels, while subtly reducing the stepping effect across the land-sea interface. NIDEM could thus provide coastal managers with near-seamless elevation data extending from inland to the ocean floor, and support a holistic approach to understanding the physical and ecological processes influencing the coastal zone. This may include providing valuable baseline elevation data for predicting the impact of coastal hazards such as storm surges or tsunami inundation (e.g. Skinner et al., 2015; Smolders et al., 2015), investigating mechanisms of coastal erosion and sediment transport (Ryu et al., 2001, 2008; Hsu et al., 2013; Gharibreza et al., 2014), or improving modelling of sea-level rise under future climate change scenarios (Galbraith et al., 2002; Thorner et al., 2014). Access to accurate intertidal elevation data is also critical for studying and conserving coastal ecosystems, particularly given the important role intertidal topography and tidal dynamics play in regulating environmental stress and spatial patterns of species richness, abundance and productivity (Scrosati et al., 2011; Valdivia et al., 2011). The outputs from NIDEM facilitate whole-of-landscape approaches to ecological modelling and three-dimensional habitat mapping in the intertidal zone that are not artificially restricted to either the marine or terrestrial domain.

A key advantage of our continental-scale approach to intertidal elevation modelling was using composite layers to identify the typical location of the waterline at various tidal heights. Intertidal zones exhibit considerable natural variability in the location of the waterline between identical tides or during ebb and flow stages (Ryu et al., 2001; Boak and Turner, 2005; Li and Gong, 2016). Wave run-up or the effect of wind can affect the location of waterlines by tens of meters on low sloping beaches or flats (Thieler and Danforth, 1994), while long-term sea-level variation, seasonal influences or storm surge events can drive

additional unpredictable variability (Boak and Turner, 2005; García-Rubio et al., 2015). Recent long-term shoreline trend studies have shown that combining multiple observations into composite layers can effectively isolate these factors, and allow waterline contours to be extracted that can be up to twice as spatially accurate as the resolution of the input satellite imagery (Almonacid-Caballer et al., 2016; Hagenaars et al., 2018). Generating median composites at ten percent increments of the tidal range allowed us to both reduce sources of natural variability and extract waterline contours that were most representative of the shoreline position across the full range of observed tidal conditions (Almonacid-Caballer et al., 2016). Using a robust central tendency median compositing method based on good quality Landsat pixel observations combined with an elevation and bathymetry filtering step also greatly reduced sensor artefacts and noise, including false positives in data-poor deeper ocean areas affected by sunglint or clouds. Issues with noise persist in some areas close to the coast, including the Archipelago of the Recherche in southern Western Australia, Port Phillip Bay in Victoria, and the south-eastern coast of Tasmania and King Island (Fig. 1). However, across most of the Australian coastline these approaches effectively eliminated the need for manually-derived masks (e.g. Chen and Chang, 2009; Murray et al., 2012) or the subjective manual selection of clear scenes (Boak and Turner, 2005). This allowed us to leverage the full Landsat archive, and facilitated the automated extraction of waterline contours at a scale that would be impractical based on manual waterline digitisation (e.g. Zhao et al., 2008). Importantly, this automated approach improves reproducibility, allowing NIDEM to be improved over time as new Landsat observations are added to the DEA platform. To facilitate reanalysis, NIDEM is released in both a 'filtered' and 'unfiltered' version, allowing users to modify or apply custom filtering to the raw data depending on their application.

3.5. Limitations and future work

The complex behaviour of tides mean that a sun synchronous sensor like Landsat does not observe the full range of the tidal cycle at all locations (Eleveld et al., 2014; Parke et al., 1987). To date, however, few studies modelling the extent and topography of the intertidal zone have addressed issues of tidal bias (e.g. Murray et al., 2012; Chen et al., 2016; Tseng et al., 2017), with the remainder implicitly assuming that satellite observations of the coastline were representative of the full local tidal range. While biases in the proportion of the tidal range observed do not affect the accuracy of absolute elevation models like NIDEM, they can prevent models from providing elevation data for areas of the intertidal zone exposed or inundated at the extremes of the tidal range. This risks giving misleading insights into the true extent of

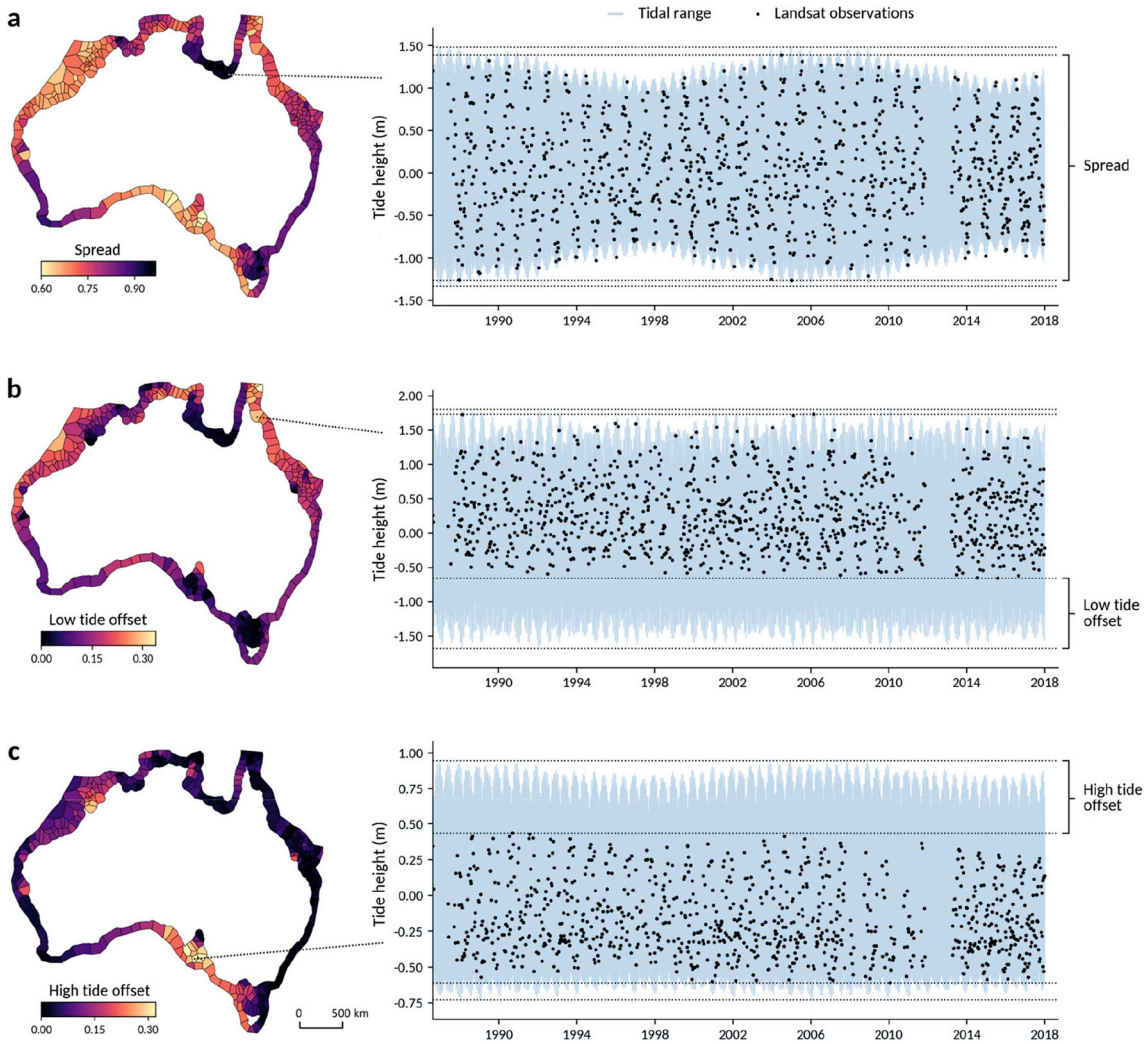

Fig. 8. The distribution of Landsat observations relative to the full tidal range. Light colours in the left panel indicate poor coverage of the tidal range by Landsat: light colours in (a) indicate polygons where Landsat observed a small 'spread' calculated as a proportion of the full tidal range. Light colours in (b) and (c) represent polygons where Landsat observations were biased away from low or high tides respectively. For example, a polygon with a spread of 0.7, a high tide offset of 0.05 and a low tide offset of 0.25 indicates that Landsat observed 70% of the tidal range, but did not image the highest 5% or lowest 25% or of tide heights.

the intertidal zone, and reduces the comparability of upper and lower elevations at different locations. The portion of the tidal cycle observed by a sun synchronous sensor can be estimated using a tidal model shown in Fig. 8. Across the Australian continent, both the overall spread of the observed tidal range compared to the full tidal range (Fig. 8a) and offsets in this proportion relative to the lowest and highest tidal extremes (Fig. 8b and c) varied greatly, even across relatively small distances in areas of rapid tidal flux. This evaluation of the observed tidal range at a particular location provides valuable information to users about the 'fitness for purpose' of NIDEM at a given location for their specific application. We strongly recommend that future regional-, continental- or global-scale intertidal zone analyses using EO data consider potential biases associated with the representativeness of their input data relative to the full tidal range. This would serve as an important first step to obtaining a better understanding of how processes driving intertidal variability affect remote sensing analyses in the intertidal zone.

Liu et al. (2013b) performed a quantitative assessment of the factors influencing the accuracy of intertidal DEMs, finding that overall DEM accuracy was strongly correlated with the number of available input satellite observations. This increase in accuracy was driven largely by the spatial coverage of waterline contours relative to total intertidal extent, with higher densities of waterline contours leading to reduced RMSE. Interpolation error represents a key source of uncertainty in waterline modelling approaches, with low contour densities increasing the proportion of the study area requiring interpolation (Mason et al., 2001; Liu et al., 2013b). The NIDEM approach based on tenth percentile tidal composites can produce relatively large spacing between waterline contours compared to waterlines digitised from individual observations, particularly in extensive shallow intertidal areas with low topographic relief (Mason et al., 2001). Rather than combining tidally tagged imagery at constant ten percent intervals of the tidal range, future work could develop an adaptive approach to composite generation tailored to the local availability of high quality satellite observations. This may result in a smaller number of higher quality tidal composites in areas with few clear observations, and a denser collection of tidal composites in areas with abundant clear observations throughout the 30-year time-series. By increasing the density of extracted waterline contours, this adaptive approach would improve the ability of the DEM to resolve finer-scale topographic features, and potentially allow high quality elevation estimates to be produced using shorter temporal extents. This may facilitate the comparison of DEMs from different temporal epochs to track and volumetrically estimate rates of coastal change (e.g. Ryu et al., 2008; Mason et al., 2010). This could be a particularly powerful approach for modelling the coastal zone if combined with additional sources of earth observation data available from satellites, such as the European Space Agency's Sentinel-2A and 2B, with a high revisit frequency compared to Landsat (approximately 5 days compared to 16 days; Drusch et al., 2012).

4. Conclusion

In this study, we have presented an automated approach to modelling the elevation of the intertidal zone based on a 30-year time series archive of Landsat remote sensing data and a multi-resolution tidal modelling framework. The resulting NIDEM dataset is to our knowledge the first continental-scale elevation model of the exposed intertidal zone, and provides an unprecedented three-dimensional representation of Australia's tidal flats, sandy beaches and shores, and rocky shores and reef environments at 25 m spatial resolution. NIDEM is based on freely available EO data and open-source software, making it directly applicable to any tidally influenced coastal environment globally. Future work will focus on integrating our approach with higher spatial and temporal resolution sources of EO data (e.g. Sentinel 2), and developing adaptive approaches to waterline contour extraction that will maximise the tidal resolution of the model based on the local availability of high quality satellite observations. This could enable modelling and comparison of finer-scale intertidal topographic features across time and at the continental-scale.

Data availability

The datasets generated in this study (Bishop-Taylor et al., 2018) and additional metadata can be accessed online (http://www.ga.gov.au/dea/products) and at the following persistent links: NIDEM 1.0 (https://doi.org/10.26186/5c4fc06a79f76) and ITEM 2.0 (https://doi.org/10.4225/25/5a602cc9eb358). Code used to generate NIDEM is available in the following repository: https://github.com/GeoscienceAustralia/nidem.

Acknowledgements

The authors would like to thank R. Nanson, F. Yuan, T. Dhu and two anonymous reviewers for their valuable and constructive comments and suggestions. We thank the individuals and organisations that provided validation data for this study. RTK GPS data used in Darwin Harbour, NT was provided by HydroSurvey Australia, with the permission of GHD and Power & Water Corporation, NT. RTK GPS data used in Moreton Bay, QLD was provided by Tim Danaher, NSW Office of Environment and Heritage. Multibeam bathymetry data over the Kimberley reefs was provided by M. O'Leary at Curtin University, WA. We thank C. Burton, S. Chua, A. Haiblen, A. Lem, B. Moushall, B. Stepin and S. Wong for assisting with field validation. This research was undertaken with the assistance of resources from the National Computational Infrastructure High Performance Data (HPD) platform, which is supported by the Australian Government. This paper is published with the permission of the Chief Executive Officer, Geoscience Australia.

Appendix A

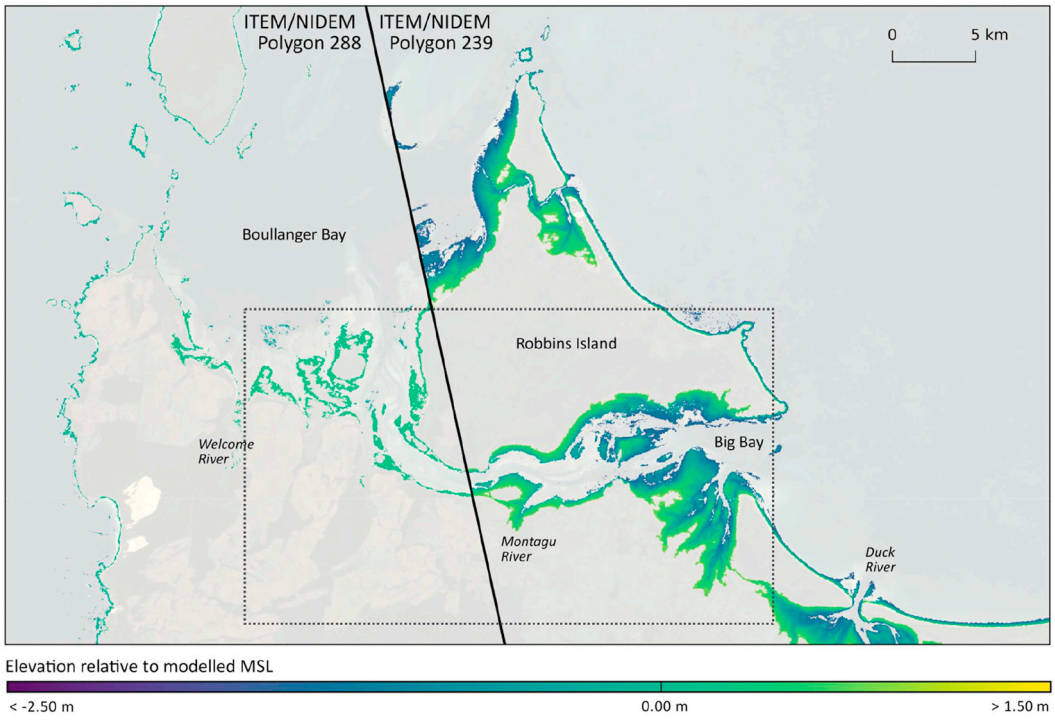

Fig. A1. Location of the Robbins Island validation site (dotted grey line), displaying the discontinuities in NIDEM elevations in Boullanger Bay at either side of the boundary of two tidal modelling polygons (dark black line)

.

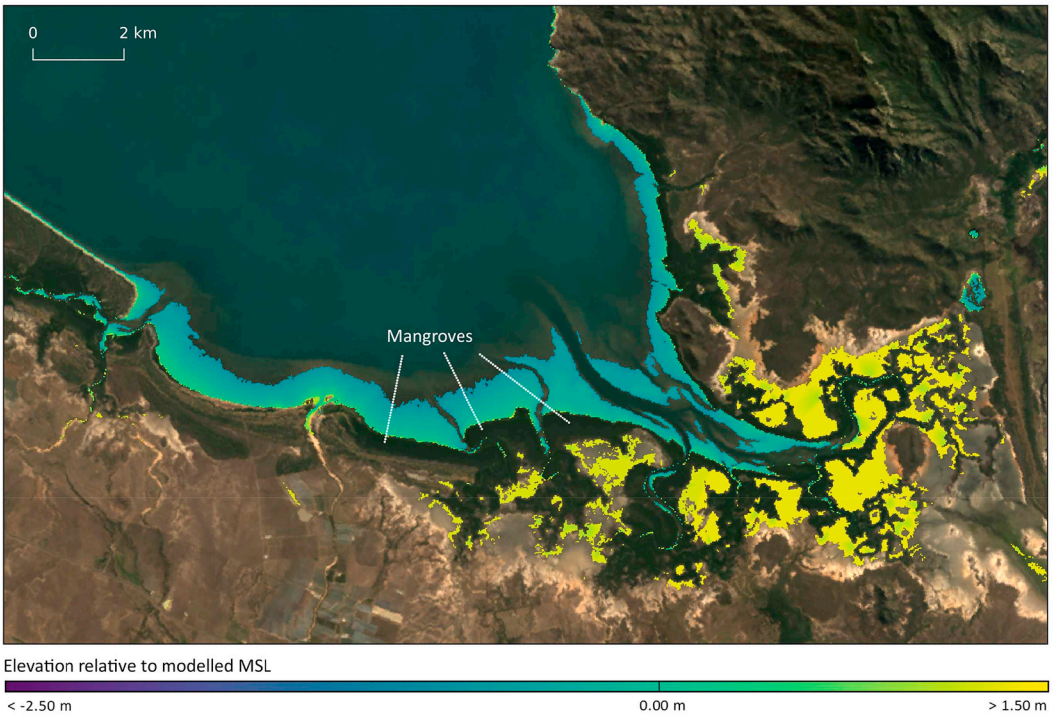

Fig. A2. NIDEM data for the Whitsunday validation site, highlighting the lack of modelled intertidal terrain in mangrove areas (dark green vegetation) and the presence of modelled elevations in areas on the landward side of mangrove communities inundated only during the highest tides.

References

Almonacid-Caballer, J., Sánchez-García, E., Pardo-Pascual, J.E., Balaguer-Beser, A.A., Palomar-Vázquez, J., 2016. Evaluation of annual mean shoreline position deduced from Landsat imagery as a mid-term coastal evolution indicator. Mar. Geol. 372, 79–88.

Banks, S.A., Skilleter, G.A., Possingham, H.P., 2005. Intertidal habitat conservation: identifying conservation targets in the absence of detailed biological information. Aquat. Conserv. Mar. Freshw. Ecosyst. 15, 271–288. https://doi.org/10.1002/aqc.683.

Barber, C.B., Dobkin, D.P., Huhdanpaa, H., 1996. The quickhull algorithm for convex hulls. ACM Trans. Math Software 22, 469–483.

Barbier, E.B., Acreman, M., Knowler, D., 1997. Economic Valuation of Wetlands: a Guide for Policy Makers and Planners. Ramsar Convention Bureau, Gland, Switzerland.

Beaman, R.J., 2018a. High-resolution Depth Model for the Great Barrier Reef - 30 M. [WWW Document]. Geoscience Australia. URL. http://pid.geoscience.gov.au/dataset/ga/115066.

Beaman, R.J., 2018b. High-resolution Depth Model for Northern Australia - 30 M. [WWW Document]. Geoscience Australia. URL. http://pid.geoscience.gov.au/dataset/ga/121620.

Bearup, D., Blasius, B., 2017. Ecotone formation induced by the effects of tidal flooding: a conceptual model of the mud flat-coastal wetland ecosystem. Ecol. Complex. 32, 217–227.

Bell, P.S., Bird, C.O., Plater, A.J., 2016. A temporal waterline approach to mapping intertidal areas using X-band marine radar. Coast. Eng. 107, 84–101. https://doi.org/10.1016/j.coastaleng.2015.09.009.

Billerbeck, M., Werner, U., Bosselmann, K., Walpersdorf, E., Huettel, M., 2006. Nutrient release from an exposed intertidal sand flat. Mar. Ecol. Prog. Ser. 316, 35–51.

Bishop-Taylor, R., Sagar, S., Lymburner, L., 2018. National Intertidal Digital Elevation Model 25m 1.0.0. [WWW Document]. Geoscience Australia. URL. https://doi.org/10.26186/5c4fc06a79f76.

Boak, E.H., Turner, I.L., 2005. Shoreline definition and detection: a review. J. Coast. Res. 688–703. https://doi.org/10.2112/03-0071.1.

Bugnot, A.B., Lyons, M.B., Scanes, P., Clark, G.F., Fyfe, S.K., Lewis, A., Johnston, E.L., 2018. A novel framework for the use of remote sensing for monitoring catchments at continental scales. J. Environ. Manag. 217, 939–950. https://doi.org/10.1016/j.jenvman.2018.03.058.

Bunt, J.S., Williams, W.T., Bunt, E.D., 1985. Mangrove species distribution in relation to tide at the seafront and up rivers. Mar. Freshw. Res. 36, 481–492.

Chen, L.C., Rau, J.Y., 1998. Detection of shoreline changes for tideland areas using multi-temporal satellite images. Int. J. Remote Sens. 19, 3383–3397.

Chen, W.-W., Chang, H.-K., 2009. Estimation of shoreline position and change from satellite images considering tidal variation. Estuar. Coast Shelf Sci. 84, 54–60. https://doi.org/10.1016/j.ecss.2009.06.002.

Chen, Y., Dong, J., Xiao, X., Zhang, M., Tian, B., Zhou, Y., Li, B., Ma, Z., 2016. Land claim and loss of tidal flats in the Yangtze Estuary. Sci. Rep. 6, 24018. https://doi.org/10.1038/srep24018.

Chmura, G.L., Anisfeld, S.C., Cahoon, D.R., Lynch, J.C., 2003. Global carbon sequestration in tidal, saline wetland soils. Glob. Biogeochem. Cycles 17.

Danaher, T., Collett, L., 2006. Development, optimisation and multi-temporal application of a simple Landsat based water index. In: Proceeding of the 13th Australasian Remote Sensing and Photogrammetry Conference, Canberra, ACT, Australia.

Dhanjal-Adams, K.L., Hanson, J.O., Murray, N.J., Phinn, S.R., Wingate, V.R., Mustin, K., Lee, J.R., Allan, J.R., Cappadonna, J.L., Studds, C.E., Clemens, R.S., Roelfsema, C.M., Fuller, R.A., 2016. The distribution and protection of intertidal habitats in Australia. Emu 116, 208. https://doi.org/10.1071/MU15046.

Dhu, T., Dunn, B., Lewis, B., Lymburner, L., Mueller, N., Telfer, E., Lewis, A., McIntyre, A., Minchin, S., Phillips, C., 2017. Digital earth Australia – unlocking new value from earth observation data. Big Earth Data 1, 64–74. https://doi.org/10.1080/20964471.2017.1402490.

Donaldson, P., Sharples, C., Anders, R.J., 2012. The Tidal Characteristics and Shallow-Marine Seagrass Sedimentology of Robbins Passage and Boullanger Bay, Far Northwest Tasmania (A Technical Report to Cradle Coast Natural Resource Management). Blue Wren Group, School of Geography and Environmental Studies, University of Tasmania, Hobart.

Drusch, M., Del Bello, U., Carlier, S., Colin, O., Fernandez, V., Gascon, F., Hoersch, B., Isola, C., Laberinti, P., Martimort, P., 2012. Sentinel-2: ESA's optical high-resolution mission for GMES operational services. Remote Sens. Environ. 120, 25–36.

Dwyer, J.L., Roy, D.P., Sauer, B., Jenkerson, C.B., Zhang, H.K., Lymburner, L., 2018. Analysis ready data: enabling analysis of the Landsat archive. Rem. Sens. 10, 1363. https://doi.org/10.3390/rs10091363.

Eakins, B.W., Grothe, P.R., 2014. Challenges in building coastal digital elevation models. J. Coast. Res. 942–953. https://doi.org/10.2112/JCOASTRES-D-13-00192.1.

Egbert, G.D., Erofeeva, S.Y., 2010. The OSU TOPEX/Poseiden Global Inverse Solution TPXO. [WWW Document]. TPXO8-atlas Version 1.0. URL. http://volkov.oce.orst.edu/tides/global.html, Accessed date: 15 February 2016.

Egbert, G.D., Erofeeva, S.Y., 2002. Efficient inverse modeling of barotropic ocean tides. J. Atmos. Ocean. Technol. 19, 183–204. https://doi.org/10.1175/1520-0426(2002)019<0183:EIMOBO>2.0.CO;2.

Egorov, A., Roy, D., Zhang, H., Hansen, M., Kommareddy, A., Egorov, A.V., Roy, D.P., Zhang, H.K., Hansen, M.C., Kommareddy, A., 2018. Demonstration of percent tree cover mapping using landsat analysis ready data (ARD) and sensitivity with respect to landsat ard processing level. Rem. Sens. 10, 209. https://doi.org/10.3390/rs10020209.

Eleveld, M.A., van der Wal, D., van Kessel, T., 2014. Estuarine suspended particulate matter concentrations from sun-synchronous satellite remote sensing: tidal and meteorological effects and biases. Remote Sens. Environ. 143, 204–215.

Fan, Y., Chen, S., Zhao, B., Yu, S., Ji, H., Jiang, C., 2018. Monitoring tidal flat dynamics affected by human activities along an eroded coast in the Yellow River Delta, China. Environ. Monit. Assess. 190, 396.

Flood, N., 2013. Seasonal composite Landsat TM/ETM+ images using the medoid (a multi-dimensional median). Rem. Sens. 5, 6481–6500.

Galbraith, H., Jones, R., Park, R., Clough, J., Herrod-Julius, S., Harrington, B., Page, G., 2002. Global climate change and sea level rise: potential losses of intertidal habitat for shorebirds. Waterbirds 25, 173–183.

Gallant, J., Dowling, T., Read, A., Wilson, N., Tickle, P., Inskeep, C., 2010. 1 Second SRTM Derived Digital Elevation Model User Guide. Geoscience Australia, Canberra, ACT.

Gao, J., 2009. Bathymetric mapping by means of remote sensing: methods, accuracy and limitations. Prog. Phys. Geogr. 33, 103–116. https://doi.org/10.1177/0309133309105657.

García-Rubio, G., Huntley, D., Russell, P., 2015. Evaluating shoreline identification using optical satellite images. Mar. Geol. 359, 96–105. https://doi.org/10.1016/j.margeo.2014.11.002.

GDAL/OGR contributors, 2018. GDAL/OGR Geospatial Data Abstraction Software Library. [WWW Document]. Open Source Geospatial Foundation. URL. http://gdal.org.

Gens, R., 2010. Remote sensing of coastlines: detection, extraction and monitoring. Int. J. Remote Sens. 31, 1819–1836. https://doi.org/10.1080/01431160902926673.

Geoscience Australia, 2015. Digital elevation model (DEM) of Australia derived from LiDAR 5 metre grid. [WWW Document]. URL. http://pid.geoscience.gov.au/dataset/ga/89644, Accessed date: 25 September 2018.

Gharibreza, M., Habibi, A., Imamjomeh, S.R., Ashraf, M.A., 2014. Coastal processes and sedimentary facies in the Zohreh river delta (northern Persian Gulf). Catena 122, 150–158.

Gorelick, N., Hancher, M., Dixon, M., Ilyushchenko, S., Thau, D., Moore, R., 2017. Google earth engine: planetary-scale geospatial analysis for everyone. Remote Sens. Environ. 202, 18–27. Big Remotely Sensed Data: tools, applications and experiences. https://doi.org/10.1016/j.rse.2017.06.031.

Hagenaars, G., de Vries, S., Luijendijk, A.P., de Boer, W.P., Reniers, A.J., 2018. On the accuracy of automated shoreline detection derived from satellite imagery: a case study of the Sand Motor mega-scale nourishment. Coast. Eng. 133, 113–125.

Hermosilla, T., Wulder, M.A., White, J.C., Coops, N.C., Hobart, G.W., 2017. Updating Landsat time series of surface-reflectance composites and forest change products with new observations. Int. J. Appl. Earth Obs. Geoinf. 63, 104–111. https://doi.org/10.1016/j.jag.2017.07.013.

Hogrefe, K.R., Wright, D.J., Hochberg, E.J., 2008. Derivation and integration of shallow-water bathymetry: implications for coastal terrain modeling and subsequent analyses. Mar. Geodes. 31, 299–317. https://doi.org/10.1080/01490410802466710.

Hsu, T.-J., Chen, S.-N., Ogston, A.S., 2013. The landward and seaward mechanisms of fine-sediment transport across intertidal flats in the shallow-water region—a numerical investigation. Cont. Shelf Res. 60, S85–S98.

HydroSurvey Australia, 2009. Report for Bathymetric and Benthic Survey of the Proposed East Point Outfall (No. Part 2), Bathymetric Report No. Survey No. 018_08. Power and Water Corporation/GHD.

Isenburg, M., 2018. LAStools-Efficient Tools for LiDAR Processing. [WWW Document]. URL. http://www.cs.unc.edu/~isenburg/lastools/.

Jones, E., Oliphant, T., Peterson, P., 2014. {SciPy}: Open Source Scientific Tools for {Python}.

Kelly, J.T., Gontz, A.M., 2018. Using GPS-surveyed intertidal zones to determine the validity of shorelines automatically mapped by Landsat water indices. Int. J. Appl. Earth Obs. Geoinf. 65, 92–104.

Kirwan, M.L., Megonigal, J.P., 2013. Tidal wetland stability in the face of human impacts and sea-level rise. Nature 504, 53–60. https://doi.org/10.1038/nature12856.

Klemas, V., 2011. Beach profiling and LIDAR bathymetry: an overview with case studies. J. Coast. Res. 1019–1028. https://doi.org/10.2112/JCOASTRES-D-11-00017.1.

Lewis, A., Lymburner, L., Purss, M.B.J., Brooke, B., Evans, B., Ip, A., Dekker, A.G., Irons, J.R., Minchin, S., Mueller, N., Oliver, S., Roberts, D., Ryan, B., Thankappan, M., Woodcock, R., Wyborn, L., 2016. Rapid, high-resolution detection of environmental change over continental scales from satellite data – the Earth Observation Data Cube. Int. J. Digital Earth 9, 106–111. https://doi.org/10.1080/17538947.2015.1111952.

Li, W., Gong, P., 2016. Continuous monitoring of coastline dynamics in western Florida with a 30-year time series of Landsat imagery. Remote Sens. Environ. 179, 196–209. https://doi.org/10.1016/j.rse.2016.03.031.

Liu, Y., Li, M., Mao, L., Cheng, L., Li, F., 2013a. Toward a method of constructing tidal flat digital elevation models with MODIS and medium-resolution satellite images. J. Coast. Res. 438–448. https://doi.org/10.2112/JCOASTRES-D-12-00088.1.

Liu, Y., Li, M., Zhou, M., Yang, K., Mao, L., 2013b. Quantitative analysis of the waterline method for topographical mapping of tidal flats: a case study in the Dongsha Sandbank, China. Rem. Sens. 5, 6138–6158. https://doi.org/10.3390/rs5116138.

Lorensen, W.E., Cline, H.E., 1987. Marching cubes: a high resolution 3D surface construction algorithm. In: ACM Siggraph Computer Graphics. ACM, pp. 163–169.

Lowe, R.J., Leon, A.S., Symonds, G., Falter, J.L., Gruber, R., 2015. The intertidal hydraulics of tide-dominated reef platforms. J. Geophys. Res. Oceans 120, 4845–4868. https://doi.org/10.1002/2015JC010701.

Luijendijk, A., Hagenaars, G., Ranasinghe, R., Baart, F., Donchyts, G., Aarninkhof, S., 2018. The state of the world's beaches. Sci. Rep. 8, 6641. https://doi.org/10.1038/s41598-018-24630-6.

Mason, D., Davenport, I., Flather, R., Gurney, C., Robinson, G., Smith, J., 2001. A sensitivity analysis of the waterline method of constructing a digital elevation model for intertidal areas in ERS SAR scene of Eastern England. Estuar. Coast Shelf Sci. 53, 759–778.

Mason, D.C., Davenport, I.J., Robinson, G.J., Flather, R.A., McCartney, B.S., 1995. Construction of an inter-tidal digital elevation model by the 'Water-Line' Method. Geophys. Res. Lett. 22, 3187–3190. https://doi.org/10.1029/95GL03168.

Mason, D.C., Hill, D., Davenport, I., Flather, R., Robinson, G., 1997. Improving inter-tidal digital elevation models constructed by the waterline technique. In: Presented at the Third ERS Symposium on Space at the Service of Our Environment, pp. 1079.

Mason, D.C., Scott, T.R., Dance, S.L., 2010. Remote sensing of intertidal morphological change in Morecambe Bay, U.K., between 1991 and 2007. Estuar. Coast Shelf Sci. 87, 487–496. https://doi.org/10.1016/j.ecss.2010.01.015.

McFeeters, S.K., 1996. The use of the Normalized Difference Water Index (NDWI) in the delineation of open water features. Int. J. Remote Sens. 17, 1425–1432. https://doi.org/10.1080/01431169608948714.

McKinney, W., 2011. pandas: a foundational Python library for data analysis and statistics. Python High Perform. Sci. Comput. 1–9.

Montgomery, J., Bryan, K., Horstman, E., Mullarney, J., 2018. Attenuation of tides and surges by mangroves: contrasting case studies from New Zealand. Water 10, 1119.

Mueller, N., Lewis, A., Roberts, D., Ring, S., Melrose, R., Sixsmith, J., Lymburner, L., McIntyre, A., Tan, P., Curnow, S., Ip, A., 2016. Water observations from space: mapping surface water from 25 years of Landsat imagery across Australia. Remote Sens. Environ. 174, 341–352. https://doi.org/10.1016/j.rse.2015.11.003.

Murray, N.J., Ma, Z., Fuller, R.A., 2015. Tidal flats of the Yellow Sea: a review of ecosystem status and anthropogenic threats. Austral Ecol. 40, 472–481. https://doi.org/10.1111/aec.12211.

Murray, N.J., Phinn, S.R., Clemens, R.S., Roelfsema, C.M., Fuller, R.A., 2012. Continental scale mapping of tidal flats across East Asia using the Landsat archive. Rem. Sens. 4, 3417–3426. https://doi.org/10.3390/rs4113417.

Murray, N.J., Phinn, S.R., DeWitt, M., Ferrari, R., Johnston, R., Lyons, M.B., Clinton, N., Thau, D., Fuller, R.A., 2018. The global distribution and trajectory of tidal flats. Nature 1.

Pardo-Pascual, J.E., Sánchez-García, E., Almonacid-Caballer, J., Palomar-Vázquez, J.M., Priego de los Santos, E., Fernández-Sarría, A., Balaguer-Beser, Á., 2018. Assessing the accuracy of automatically extracted shorelines on microtidal beaches from Landsat 7, Landsat 8 and Sentinel-2 imagery. Rem. Sens. 10, 326.

Parke, M.E., Stewart, R.H., Farless, D.L., Cartwright, D.E., 1987. On the choice of orbits for an altimetric satellite to study ocean circulation and tides. J. Geophys. Res.: Oceans 92, 11693–11707.

Purcell, S., 2002. Intertidal reefs under extreme tidal flux in Buccaneer Archipelago, Western Australia. Coral Reefs 21, 191–192.

Roberts, D., Mueller, N., McIntyre, A., 2017. High-dimensional pixel composites from Earth Observation time series. IEEE Trans. Geosci. Remote Sens. 1–11. https://doi.org/10.1109/TGRS.2017.2723896.

Rodríguez, J.F., Saco, P.M., Sandi, S., Saintilan, N., Riccardi, G., 2017. Potential increase in coastal wetland vulnerability to sea-level rise suggested by considering hydrodynamic attenuation effects. Nat. Commun. 8, 16094.

Rogers, K., Lymburner, L., Salum, R., Brooke, B.P., Woodroffe, C.D., 2017. Mapping of mangrove extent and zonation using high and low tide composites of Landsat data. Hydrobiologia 803, 49–68. https://doi.org/10.1007/s10750-017-3257-5.

Ryu, J.-H., Cho, W.-J., Won, J.-S., 2001. Estimation of the sedimentation budget in tidal flat using remotely sensed data. In: Presented at the Geoscience and Remote Sensing Symposium, 2001. IGARSS'01. IEEE 2001 International, IEEE, pp. 2409–2411.

Ryu, J.-H., Kim, C.-H., Lee, Y.-K., Won, J.-S., Chun, S.-S., Lee, S., 2008. Detecting the intertidal morphologic change using satellite data. Estuar. Coast Shelf Sci. 78, 623–632. https://doi.org/10.1016/j.ecss.2008.01.020.

Ryu, J.-H., Won, J.-S., Min, K.D., 2002. Waterline extraction from Landsat TM data in a tidal flat: a case study in Gomso Bay, Korea. Remote Sens. Environ. 83, 442–456. https://doi.org/10.1016/S0034-4257(02)00059-7.

Sagar, S., Phillips, C., Bala, B., Roberts, D., Lymburner, L., 2018. Generating continental scale pixel-based surface reflectance composites in coastal regions with the use of a multi-resolution tidal model. Rem. Sens. 10, 480. https://doi.org/10.3390/rs10030480.

Sagar, S., Roberts, D., Bala, B., Lymburner, L., 2017. Extracting the intertidal extent and topography of the Australian coastline from a 28 year time series of Landsat observations. Remote Sens. Environ. 195, 153–169. https://doi.org/10.1016/j.rse.2017.04.009.

Scrosati, R.A., Knox, A.S., Valdivia, N., Molis, M., 2011. Species richness and diversity across rocky intertidal elevation gradients in Helgoland: testing predictions from an environmental stress model. Helgol. Mar. Res. 65, 91.

Serra, J., 1983. Image Analysis and Mathematical Morphology. Academic Press, Inc.

Sharples, C., Mount, R., Pedersen, T., 2009. The Australian Coastal Smartline Geomorphic and Stability Map Version 1: Manual and Data Dictionary. Report of the University of Tasmania for the Department of Climate Change and Geoscience Australia.

Skinner, C.J., Coulthard, T.J., Parsons, D.R., Ramirez, J.A., Mullen, L., Manson, S., 2015. Simulating tidal and storm surge hydraulics with a simple 2D inertia based model. In: The Humber Estuary, UK. Estuarine, Coastal and Shelf Science, vol 155. pp. 126–136.

Smolders, S., Plancke, Y., Ides, S., Meire, P., Temmerman, S., 2015. Role of intertidal wetlands for tidal and storm tide attenuation along a confined estuary: a model study. Nat. Hazards Earth Syst. Sci. 15, 1659–1675.

Solihuddin, T., O'Leary, M.J., Blakeway, D., Parnum, I., Kordi, M., Collins, L.B., 2016. Holocene reef evolution in a macrotidal setting: Buccaneer Archipelago, Kimberley Bioregion, northwest Australia. Coral Reefs 1–12. https://doi.org/10.1007/s00338-016-1424-1.

Spruzen, F.L., Richardson, A.M., Woehler, E.J., 2008. Spatial variation of intertidal macroinvertebrates and environmental variables in Robbins Passage wetlands, NW Tasmania. Hydrobiologia 598, 325–342.

Su, H., Liu, H., Heyman, W.D., 2008. Automated derivation of bathymetric information from multi-spectral satellite imagery using a non-linear inversion model. Mar. Geodes. 31, 281–298. https://doi.org/10.1080/01490410802466652.

Temmerman, S., Meire, P., Bouma, T.J., Herman, P.M., Ysebaert, T., De Vriend, H.J., 2013. Ecosystem-based coastal defence in the face of global change. Nature 504, 79.

Thieler, E.R., Danforth, W.W., 1994. Historical shoreline mapping (I): improving techniques and reducing positioning errors. J. Coast. Res. 549–563.

Thorner, J., Kumar, L., Smith, S.D., 2014. Impacts of climate-change-driven sea level rise on intertidal rocky reef habitats will be variable and site specific. PLoS One 9, e86130.

Tseng, K.-H., Kuo, C.-Y., Lin, T.-H., Huang, Z.-C., Lin, Y.-C., Liao, W.-H., Chen, C.-F., 2017. Reconstruction of time-varying tidal flat topography using optical remote sensing imageries. ISPRS J. Photogrammetry Remote Sens. 131, 92–103. https://doi.org/10.1016/j.isprsjprs.2017.07.008.

Valdivia, N., Scrosati, R.A., Molis, M., Knox, A.S., 2011. Variation in community structure across vertical intertidal stress gradients: how does it compare with horizontal variation at different scales? PLoS One 6, e24062.

Van der Walt, S., Schönberger, J.L., Nunez-Iglesias, J., Boulogne, F., Warner, J.D., Yager, N., Gouillart, E., Yu, T., 2014. scikit-image: image processing in Python. PeerJ 2, e453.

Wang, X., Xiao, X., Zou, Z., Chen, B., Ma, J., Dong, J., Doughty, R.B., Zhong, Q., Qin, Y., Dai, S., 2018. Tracking annual changes of coastal tidal flats in China during 1986–2016 through analyses of Landsat images with Google Earth Engine. Remote Sens. Environ. https://doi.org/10.1016/j.rse.2018.11.030.

Weatherall, P., Marks, K.M., Jakobsson, M., Schmitt, T., Tani, S., Arndt, J.E., Rovere, M., Chayes, D., Ferrini, V., Wigley, R., 2015. A new digital bathymetric model of the world's oceans. Earth Space Sci. 2, 331–345. https://doi.org/10.1002/2015EA000107.

White, J.C., Wulder, M.A., Hobart, G.W., Luther, J.E., Hermosilla, T., Griffiths, P., Coops, N.C., Hall, R.J., Hostert, P., Dyk, A., Guindon, L., 2014. Pixel-Based Image compositing for large-area dense time series applications and science. Can. J. Remote Sens. 40, 192–212. https://doi.org/10.1080/07038992.2014.945827.

Whiteway, T., 2009. Australian Bathymetry and Topography Grid. Geoscience Australia, Canberra. http://pid.geoscience.gov.au/dataset/ga/67703.

Williams, R.J., Watford, F.A., 1997. Identification of structures restricting tidal flow in New South Wales, Australia. Wetl. Ecol. Manag. 5, 87–97.

Woodcock, C.E., Allen, R., Anderson, M., Belward, A., Bindschadler, R., Cohen, W., Gao, F., Goward, S.N., Helder, D., Helmer, E., Nemani, R., Oreopoulos, L., Schott, J., Thenkabail, P.S., Vermote, E.F., Vogelmann, J., Wulder, M.A., Wynne, R., 2008. Free access to Landsat imagery. Science 320 1011–1011. https://doi.org/10.1126/science.320.5879.1011a.

Wulder, M.A., Masek, J.G., Cohen, W.B., Loveland, T.R., Woodcock, C.E., 2012. Opening the archive: how free data has enabled the science and monitoring promise of Landsat. Remote Sens. Environ. 122, 2–10. Landsat Legacy Special Issue. https://doi.org/10.1016/j.rse.2012.01.010.

Xia, S., Yu, X., Millington, S., Liu, Y., Jia, Y., Wang, L., Hou, X., Jiang, L., 2017. Identifying priority sites and gaps for the conservation of migratory waterbirds in China's coastal wetlands. Biol. Conserv. 210, 72–82. Special Issue on China's Biodiversity Conservation. https://doi.org/10.1016/j.biocon.2016.07.025.

Xu, H., 2006. Modification of normalised difference water index (NDWI) to enhance open water features in remotely sensed imagery. Int. J. Remote Sens. 27, 3025–3033. https://doi.org/10.1080/01431160600589179.

Xu, N., 2018. Detecting coastline change with all available landsat data over 1986–2015: a case study for the state of Texas, USA. Atmosphere 9, 107.

Xu, Z., Kim, D., Kim, S.H., Cho, Y.-K., Lee, S.-G., 2016. Estimation of seasonal topographic variation in tidal flats using waterline method: a case study in Gomso and Hampyeong Bay, South Korea. Estuar. Coast Shelf Sci. 183, 213–220. https://doi.org/10.1016/j.ecss.2016.10.026.

Zhao, B., Guo, H., Yan, Y., Wang, Q., Li, B., 2008. A simple waterline approach for tidelands using multi-temporal satellite images: a case study in the Yangtze Delta. Estuar. Coast Shelf Sci. 77, 134–142. https://doi.org/10.1016/j.ecss.2007.09.022.